ACS NANO
Cite This: ACS Nano 2019, 13, 5816−5825
www.acsnano.org

ARTICLE

Redox-Activatable and Acid-Enhanced Nanotheranostics for Second Near-Infrared Photoacoustic Tomography and Combined Photothermal Tumor Therapy

Zhimin Wang,[†] Xu Zhen,[‡] Paul Kumar Upputuri,[‡] Yuyan Jiang,[‡] Junwei Lau,[†] Manojit Pramanik,[‡] Kanyi Pu,*[,‡] and Bengang Xing*[,†]

[†]Division of Chemistry and Biological Chemistry, School of Physical & Mathematical Sciences, Nanyang Technological University, 21 Nanyang Link, 637371, Singapore

[‡]School of Chemical and Biomedical Engineering, Nanyang Technological University, 70 Nanyang Drive, 637459, Singapore

Supporting Information

ABSTRACT: **Tumor phototheranostics in the second near-infrared window (NIR-II, 1000−1700 nm) holds great promise due to high spatiotemporal precision, enhanced penetration depth, and therapeutic efficacy. However, current "always-on" NIR-II phototheranostic agents remain restricted by the inherent nonspecificity from the pseudosignal readout and undesirable treatment-related side effects. To address these challenges, herein we explore an activatable and biocompatible nanotheranostics that generates diagnostic and therapeutic effects only after specific activation and enhancement by tumor microenvironmental redox and acid while keeping silent at normal tissues. Such an intelligent "turn-on" chromogenic nanotheranostics allows *in vivo* nearly zero-background photoacoustic tomography (PAT) and combined effective photothermal tumor therapy (PTT) both in the NIR-II range with minimal adverse effects. In light of the high sensitivity, superior penetration depth, and biocompatibility, this stimuli-activatable NIR-II photo-nanotheranostics provides broad prospects for the investigation and intervention of deep-tissue redox and acid-associated physiological and pathological events.**

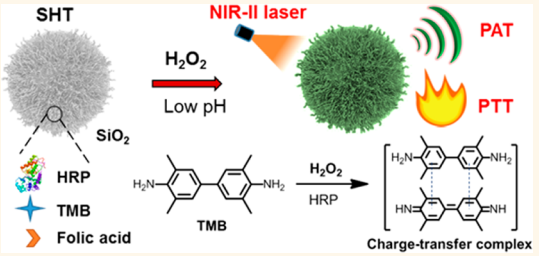

KEYWORDS: *tumor microenvironment, activatable nanotheranostics, second near-infrared window, photoacoustic tomography, photothermotherapy*

In the past few years, significant advances in near-infrared (NIR) light-mediated nanoplatforms ranging from organic dye assemblies, semiconducting polymers, and carbon nanotubes to inorganic metallic gold nanoparticles, quantum dots, and upconversion nanoparticles have highly promoted the developments of phototheranostics for the healthcare and life sciences.[1−3] These NIR nanotheranostic agents hold great promise in personalized medicine due to their simultaneous disease diagnosis and therapy with specific targeting, deep-tissue penetration, high spatiotemporal precision, and minimal invasiveness.[1,4−7] As an emerging phototheranostic modality, NIR photoacoustic tomography (PAT) and its combined photothermal therapy (PTT) have gained considerable interest in recent tumor treatment research.[8−12] Compared with most NIR-I (650−1000 nm) phototheranostics, some NIR-II window (1000−1700 nm) theranostic studies have validated that both PAT and PTT in this wavelength range exhibit a superior signal-to-noise ratio (SNR) and enhanced treatment efficacy.[13−25] However, despite these great promises, current "always-on" NIR-II phototheranostic agents remain restricted by the inherent nonspecificity from the pseudosignal readout and undesirable treatment-related side effects.

To address these challenges, exploring the environment-activatable "turn-on" NIR-II phototheranostics that generates diagnostic and therapeutic effects only after specific activation in a tumorous area while keeping silent at normal tissues could be an effective strategy.[26−28] In view of the intrinsic complexity of tumor physiology, tumor microenvironment (TME) characteristics (*e.g.*, high redox state, low pH, hypoxia) have attracted tremendous attention for the rational design of stimuli-responsive, on-demand, and effective tumor theranostic agents.[29−33] Although several microenvironmental stimuli-activatable NIR-II fluorescent nanoplatforms have been

Received: February 19, 2019
Accepted: April 29, 2019
Published: April 29, 2019

DOI: 10.1021/acsnano.9b01411
ACS Nano 2019, 13, 5816−5825

Scheme 1. Illustration of SHT Formation and Its H_2O_2 Activation and Acid Enhancement for Tumor-Specific NIR-II Photonanotheranostics

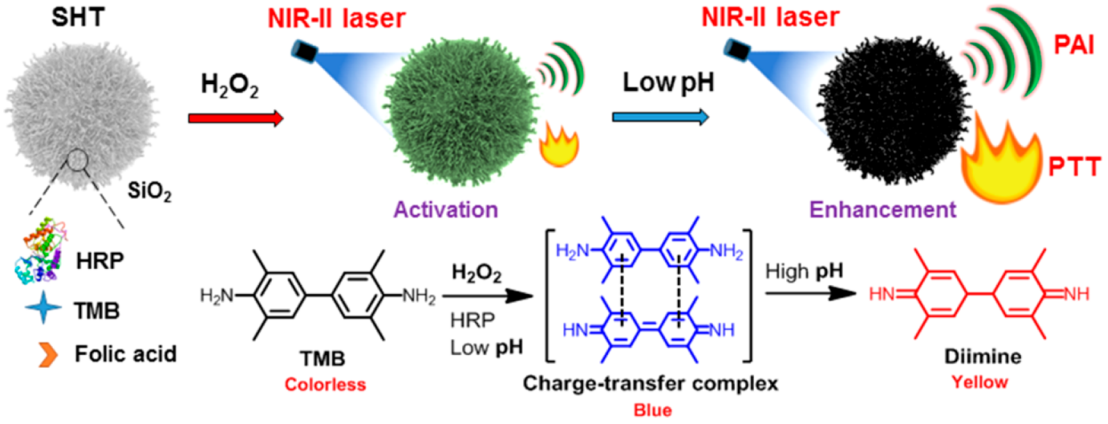

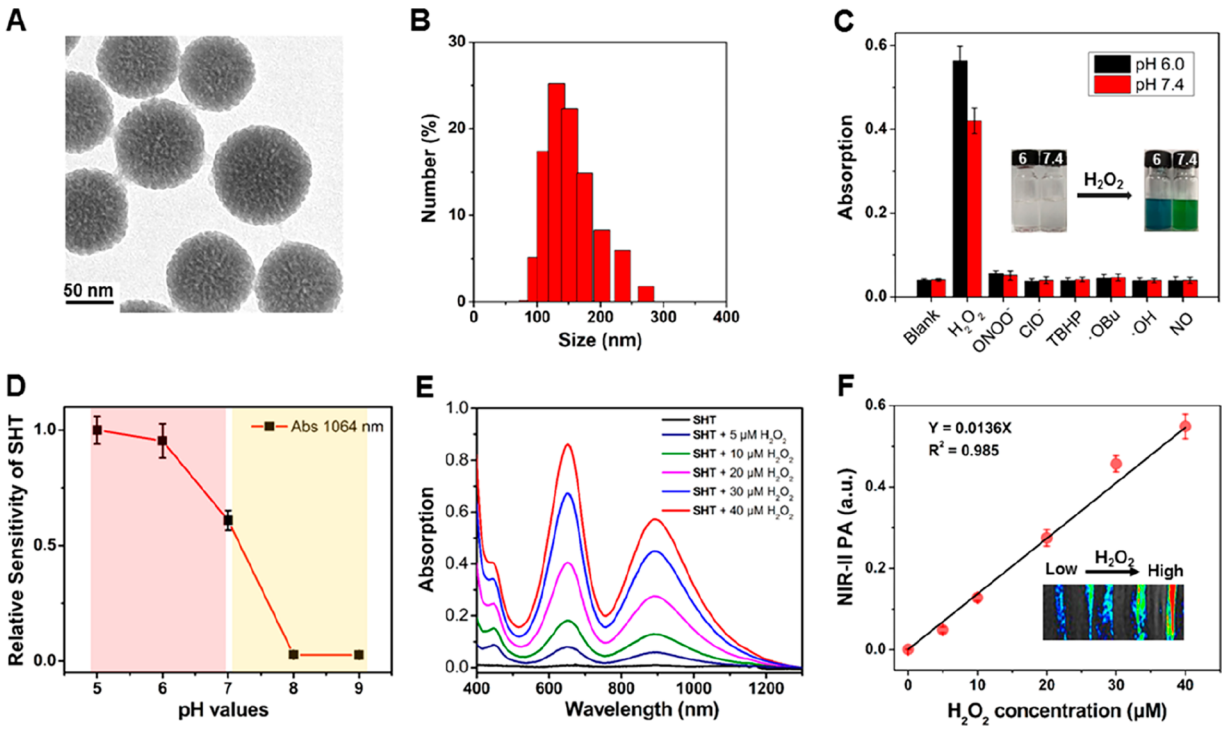

Figure 1. Preparation and characterization of the activatable nanotheranostics SHT. (A) TEM image of prepared SHT. (B) Size distribution of SHT nanospheres in water determined by dynamic light scattering. (C) Absorbance of SHT at 1064 nm after incubation with various types of free radical species (25 μM) for 10 min. (D) Determination of SHT sensitivity for H_2O_2 detection in different pH buffers. (E) UV−vis−NIR absorbance spectra of SHT (0.1 mg/mL) with different H_2O_2 concentrations in PBS buffer. (F) PA imaging and signal plot at 1064 nm as a function of the concentration of H_2O_2.

successfully constructed and applied in tumor detection and guided phototherapy,[34−36] it should be noted that these NIR-II emissive systems were actually excited by a NIR-I (*e.g.*, 800 nm) laser for imaging and therapeutic purposes in practice. Particularly, the activatable phototheranostics with higher efficacy and deeper tissue penetration of PA sensing as well as combined PTT both in the NIR-II window has not been fully developed to date.

In view of our previous results, the broadband absorbing and biodegradable charge-transfer complex (CTC) by 3,3′,5,5′-tetramethylbenzidine (TMB) oxidation not only possesses strong NIR-II (1064 nm) PA signal but also can specifically respond to an environmental pH change.[37] Although such a promising pH-sensitive NIR-II PA probe allows tumor acidity imaging, the sensitivity, targeting specificity, and the administration mode are worthy of further refinements. In this study, we report an evolutionary version of tumor microenvironment-activated nanotheranostics (SHT, SiO_2@HRP/TMB) for precise PAT and combined PTT both in the NIR-II window. This intelligent chromogenic nanotheranostics is fabricated by a tumor folate (folic acid, FA)-specific modified mesoporous silica nanocarrier that is simultaneously loaded with the enzyme horseradish peroxidase (HRP) and its substrate, TMB, enabling specific "turn-on" response by the key tumor microenvironmental redox parameter, H_2O_2.[38,39] Once reaching the tumor area, the colorless SHT nanoprobe could be converted to the strong broadband-absorbing form with the wavelength ranging from the visible to the NIR-II

DOI: 10.1021/acsnano.9b01411
ACS Nano 2019, 13, 5816−5825

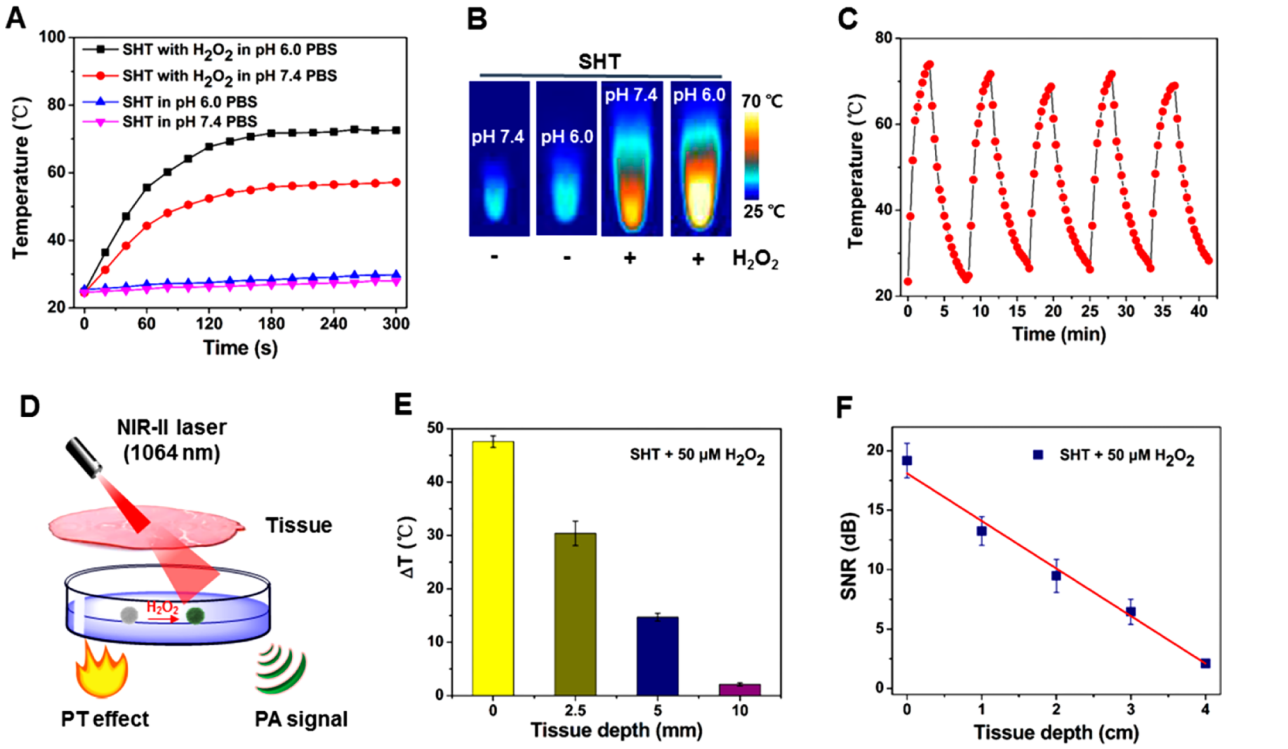

Figure 2. ***In vitro*** **photothermal and photoacoustic studies of SHT with or without H_2O_2 in different pH conditions. (A, B) Temperature increase and IR thermal images of SHT (0.1 mg/mL) in different pH PBS buffers with or without H_2O_2 (50 μM) incubation under 1064 nm laser irradiation (1.0 W/cm^2). (C) Photostability study of SHT after H_2O_2 response in pH 6.0 PBS buffer by reversible photothermal heating and natural cooling cycles. (D) Schematic illustration of deep-tissue NIR-II PT and PA studies of SHT after H_2O_2 response. (E) Temperature changes of H_2O_2-incubated SHT at different tissue depths under 1064 nm laser irradiation (1.0 W/cm^2). (F) Plot of photoacoustic SNR with H_2O_2-incubated SHT at 1064 nm as a function of the tissue depth. Laser energy density was 20 mJ/cm^2.**

window; meanwhile the chromogenic response would be significantly amplified in the acidic condition owing to the relatively high HRP activity and better stability of CTC than that at neutral physiological pH.[37,40,41] Such an intelligent H_2O_2-activable and acid-enhanced nanotheranostics allows *in vivo* nearly-zero-background PA tumor tomography and combined effective PTT with NIR-II light irradiation (Scheme 1). Considering the high sensitivity, superior penetration depth, and excellent biocompatibility, this NIR-II photo-nanotheranostics holds broad prospects for the investigation and intervention of deep-tissue H_2O_2 production and acid-associated physiological and pathological events.

RESULTS AND DISCUSSION

As indicated in Scheme 1 and Figure S1A, to construct the activatable SHT nanotheranostics, we first prepared 3D dendritic biodegradable and amino-functionalized mesoporous silica nanospheres according to the heterogeneous oil−water biphase stratification reaction strategy.[42] Transmission electron microscopy (TEM) observation clearly revealed that the as-prepared SiO_2 nanospheres feature a dendritic hierarchical mesostructure (Figure S1B). To further fabricate the tumor-specific nanotheronostics, folic acid as a targeting ligand was subsequently modified on the surface of SiO_2 ($-NH_2$) by the coupling reaction between $-COOH$ and $-NH_2$ groups.[43] Then the HRP and TMB were encapsulated into the pores of mesoporous silica-based nanocarriers through the processes of physical diffusion and adsorption.[44,45] The TEM image in Figure 1A indicates the formation of nanocompositions for the obtained SiO_2@HRP/TMB (SHT), which showed mono-dispersed, uniform spherical frameworks with the average diameter distribution verified to be 145.5 nm by dynamic light scattering (DLS) measurement (Figure 1B). Spectral differences in the FTIR characterization (Figure S1C) between SiO_2, SiO_2−FA, and SiO_2−FA−TMB could also be direct evidence for the successful modifications. The loading efficacy of FA, TMB, and HRP was determined to be 12.7%, 19.9%, and 2.47% by using absorption spectroscopy, respectively (Figure S2).

The HRP/TMB-based colorimetric assay has been extensively applied for reactive oxygen species (ROS, *e.g.*, H_2O_2) sensing as well as the enzyme-linked immunosorbent assay (ELISA) in biochemical research.[41,46] In view of our "turn-on" activatable nanotheranostics, the chromogenic substrate TMB and the catalase HRP were encapsulated into SHT as an integrated colorimetric assay system, which enabled the capability of sensitive detection of environmental H_2O_2. The sensing specificity of SHT was evaluated by incubation with various radical species, including H_2O_2, peroxynitrite ($ONOO^-$), hypochlorite (^-OCl), *tert*-butyl hydroperoxide (TBHP), *tert*-butoxy radical (•OtBu), hydroxyl radical (•OH), and nitric oxide (NO). Notably, only the SHT and H_2O_2 co-incubated group showed strong NIR-II absorbance at 1064 nm, whereas no significant color response was found in the groups with any other types of free radical incubation (Figure 1C). Moreover, the absorbance change of SHT toward H_2O_2 in the slightly acidic condition (pH 6.0) was more obvious than those in the neutral condition (pH 7.4). To further validate the sensitivity of SHT activation in various pH environments, the pH-dependent absorption responses of SHT

DOI: 10.1021/acsnano.9b01411
ACS Nano 2019, 13, 5816−5825

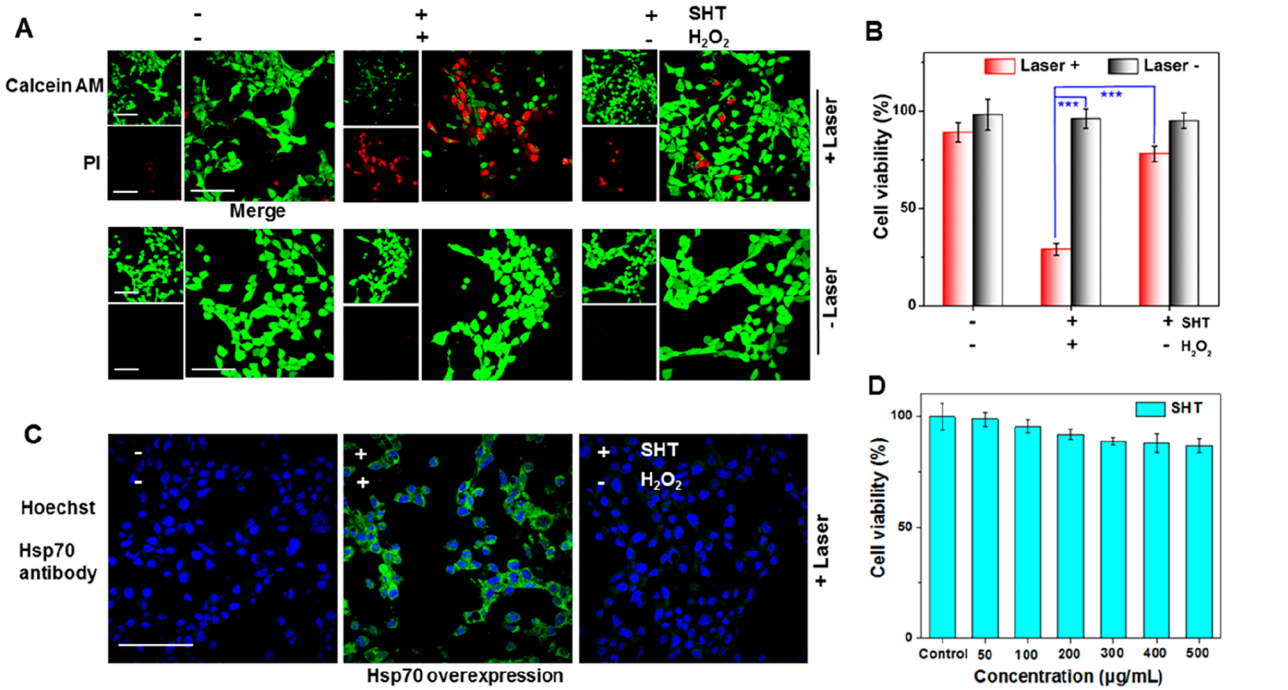

Figure 3. NIR-II PT study in cells. (A) Confocal fluorescence images of SHT-incubated 4T1 cells after laser irradiation at 1064 nm (1 W/cm^2) for 6 min. Live/dead stain shows dead cells as red and viable cells as green. Scale bars, 100 μm. (B) Viability test of photothermal destruction of 4T1 cells. (C) Hsp70-expression analysis of 4T1 cells treated with SHT and activated by H_2O_2 upon 1064 nm irradiation (1 W/cm^2, 6 min). Treated 4T1 cells were stained with Alexa Fluor 488 labeled anti-Hsp70 antibody. Scale bars, 100 μm. (D) Cytotoxicity of different concentrations SHT against 4T1 cells.

toward H_2O_2 were measured in varying pH buffers ranging from 5.0 to 9.0. The results indicated that SHT exhibited high sensitivity in acidic buffers in the presence of H_2O_2, while the response in the basic condition was extremely slow (Figures 1D and S3A). Additionally, the strong NIR-II absorbance of the H_2O_2/SHT solution in acidic condition (pH 6.0) remained unchanged even after 24 h; however, the absorption of the same sample at pH 7.4 almost entirely disappeared due to the biodegradability of the generated charge-transfer complex (Figure S3B).

To determine the feasibility of H_2O_2 sensing by using the PAT modality, SHT solutions with different concentrations of H_2O_2 were tested for both absorbance and PA signal changes. As shown in Figure 1E, the absorbance increase was found to be H_2O_2-concentration-dependent. Moreover, the linear correlation between the concentration of H_2O_2 and the NIR-II PA amplitude was observed in Figure 1F, indicating the potential applicability for quantitative H_2O_2 detection. Considering a high-redox and acidic microenvironment in solid tumors due to the increased glycolytic metabolism, deficient blood perfusion, and the processes of hypoxia,[47,48] such a H_2O_2-activated and acidity-enhanced nanotheranostics holds promising potentials for further applications of tumor-specific activatable diagnostics and therapeutics.

The broadband NIR-absorbing feature of SHT upon H_2O_2 action not only enables a good NIR-II absorber for PAT but also may serve as a photothermal agent for *in vivo* tumor PTT. Notably, very recent research has demonstrated that TMB-oxidation-based CTC showed a strong NIR-laser-driven photothermal effect and the TMB–H_2O_2 colorimetric system could be potentially used for photothermal immunoassay.[49] We examined the photothermal property of SHT upon H_2O_2 activation by NIR-II laser (1064 nm) irradiation at a power density of 1.0 W/cm^2. As shown in Figure 2A and B, the IR thermal camera images clearly showed dramatic temperature increases with the blue-colored H_2O_2-incubated SHT solutions after 5 min of irradiation. However, no obvious temperature change was found with the colorless SHT solutions in the absence of H_2O_2. Furthermore, there was obvious enhanced photothermal heating effect observed in the acidic SHT–H_2O_2 reaction solution (pH 6.0) than that in the neutral condition (pH 7.4) with the same NIR-II irradiation, indicating the excellent photothermal specificity for potential tumor-selective PTT without the normal tissue damage caused by nonspecific overheating. Moreover, the H_2O_2-activated SHT solution exhibited superior photothermal stability (Figure 2C), which reveals the possibility for potential *in vivo* PTT studies.

To validate the deep-tissue penetration performances of NIR-II PAT and photothermal effects, a homemade PAT system and a tissue-mimicking phantom covered with different thicknesses of chicken breast muscles were used to test the penetrating features (Figures 2D and S4A,D).[16] The results in Figure 2E demonstrated tissue-depth-dependent temperature decreases of H_2O_2-activated SHT solutions under 10 min of 1064 nm laser irradiation (1.0 W/cm^2). It should be noted that a 14.7 °C extra temperature increase was observed with the 5 mm tissue depth covered SHT/H_2O_2 sample; such heating enhancement was sufficient to ablate tumor cells according to the threshold temperature increase (10–13 °C) for *in vivo* PTT.[50] However, 808 nm laser irradiation for this sample with 5 mm tissue blocking only induced a tiny temperature change at the same power intensity (Figure S4E). Additionally, the deep-tissue 1064 nm PA signals of H_2O_2-activated SHT solutions were examined and plotted in Figure 2F. Although the SNR of the irradiated samples gradually decreased along with the tissue depth increasing from 0 to 4 cm, a clear PA

DOI: 10.1021/acsnano.9b01411
ACS Nano 2019, 13, 5816–5825

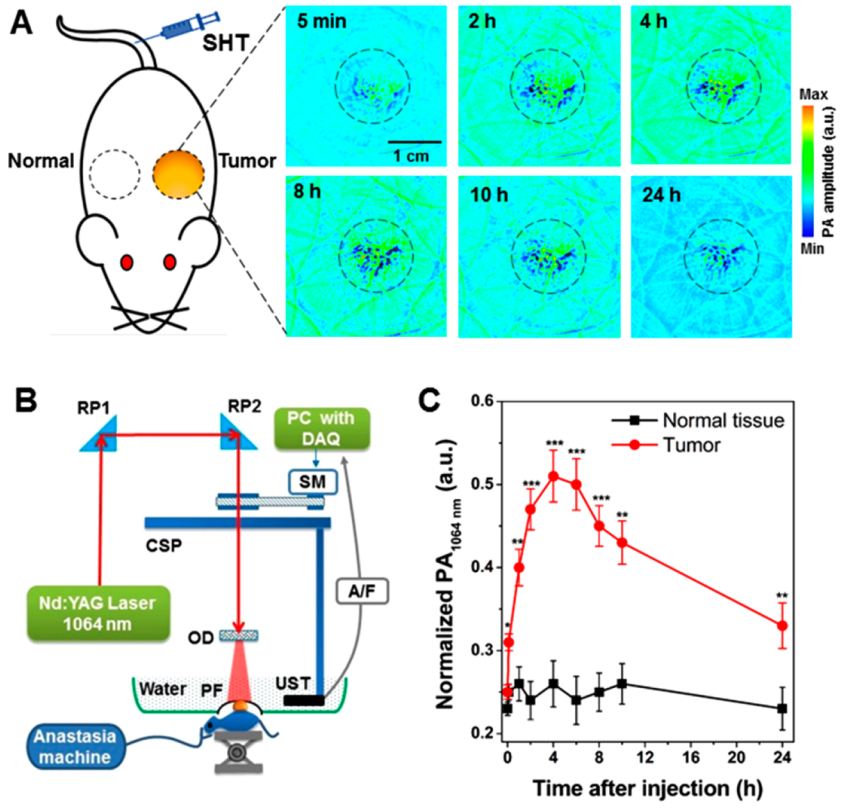

Figure 4. ***In vivo*** **NIR-II PA tumor detection. (A) Representative PA images of the 4T1-tumor-bearing mice postinjection of SHT (2 mg/mL, 200 μL). (B) Schematic diagram of 1064 nm Nd:YAG laser based PAT system. Here, RP = right angle prism, CRD = circular rotating disc, SM = stepper motor, DAQ = data acquisition card, RFA = ultrasound receiver/filter/amplifier unit, UST = ultrasound transducer, OD = optical diffuser, PF = 100 μm transparent polythene membrane. (C) Normalized mean PA amplitudes as a function of SHT postinjection time. Energy density of 1064 nm pulse laser irradiation, 5.5 mJ/cm^2. Statistically significant difference in PA amplitude (au) between tumor and normal tissue (*p < 0.05, **p < 0.01, ***p < 0.001, n = 3).**

contrast was still detectable (SNR, ∼10 dB) even up to a 2 cm tissue depth. Further comparative deep-tissue penetrating studies between typical NIR-I (800 nm) and NIR-II (1064 nm) lasers also indicated the superiority of NIR-II PAT (Figure S4B and C). These results demonstratively proved the excellent tissue-penetrating capabilities of both PAT and PT effects in the NIR-II window.

To further look into the specificity and capability of NIR-II photothermal tumor cell ablation by H_2O_2-activated SHT nanotheranostics, 4T1 cells were incubated with 0.1 mg/mL of SHT for 4 h, and the culture medium was removed, then replenished with a fresh one without or with 50 μM H_2O_2 to mimic the normal or tumor redox microenvironment. After 1 h of incubation, the cells were irradiated for 6 min with a 1064 nm laser (1.0 W/cm^2). The PTT efficacy was evaluated by live/dead cells staining (calcein AM and propidium iodide) and quantitatively measured through using the resazurin-based cell viability assay. As shown in Figure 3A, B, and D, there was no obvious cytotoxicity in both SHT and H_2O_2 treatment groups without laser irradiation, while remarkable dead cell staining and much lower viability (29.7%) were observed in the SHT/H_2O_2 co-incubated group after the photoirradiation. Moreover, a significant difference of cell viability was found between H_2O_2-treated and control (no H_2O_2 treatment) groups with combined SHT/NIR-II laser operations, indicating that such effective photothermal damage was specifically activated by H_2O_2. These results clearly demonstrated the selective photothermal tumor-cell-killing ability of our activatable nanotheranostics. In an attempt to clarify the potential mechanism of this H_2O_2-activated SHT in PTT, we analyzed the expression level of thermal-stress-associated heat shock protein 70 (Hsp70) in 1064 nm laser irradiated 4T1 cells.[51] After the immunofluoresent staining by Alexa Fluor 488 anti-Hsp70 antibody, an obvious green fluorescence was observable in SHT−H_2O_2-treated cells (Figure 3C), which confirmed the heat-induced Hsp70 overexpression. In contrast, 4T1 cells with either SHT or H_2O_2 treatment only showed relatively low Hsp70 expression after the same photoirradiation. These results further validated the NIR-II PTT-triggered tumor cell response specifically derived from the external heat stimuli that was generated by H_2O_2-activated SHT.

In order to evaluate the capability of SHT for NIR-II PA H_2O_2 sensing in the tumor microenvironment, the 4T1-tumor-bearing mouse model was established by following the standard protocol;[52] then mice administrated with SHT (200 μL, 2 mg/mL) *via* tail vein injection were scanned on a homemade PAT setup with 1064 nm pulsed laser excitation (Figure 4A and B). The PA signals of the tumor area at one back side gradually increased over time, which indicated the formation of the broadband-absorbing CTC derived from the SHT response toward tumorous H_2O_2. However, no obvious enhanced PA contrast except for the background noise appeared in the normal tissue at different time periods after SHT injection (Figures 4C and S5). It was noted that the 1064 nm PA signal reached a plateau after SHT injection at 4−6 h,

DOI: 10.1021/acsnano.9b01411
ACS Nano 2019, 13, 5816−5825

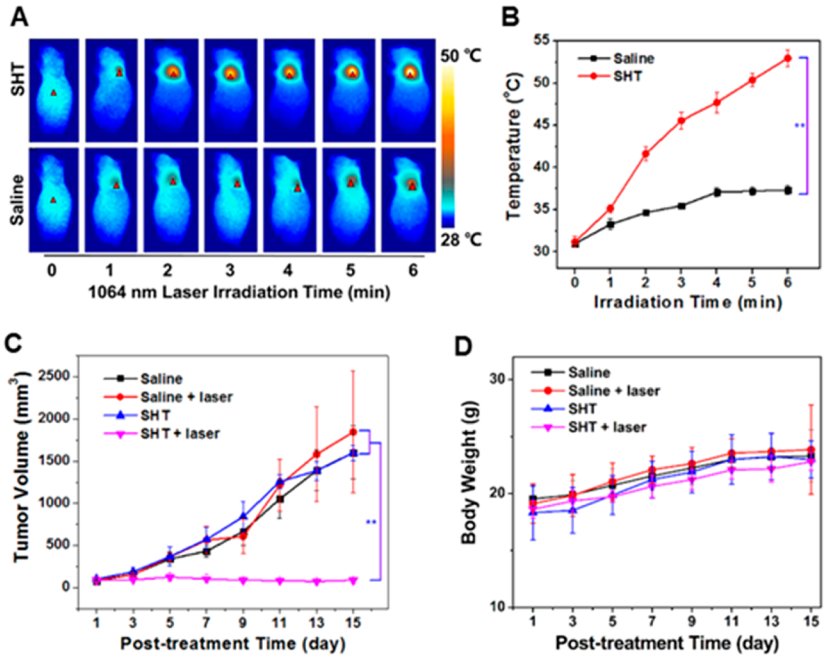

Figure 5. *In vivo* **NIR-II PTT against tumor. (A) IR thermal images of 4T1-tumor-bearing mice with intravenous injection of SHT under laser irradiation at 1064 nm (1 W/cm^2) for different times. (B) Temperature changes during laser irradiation after intravenous injection of saline and SHT into 4T1-tumor-bearing mice (**$p < 0.01$, $n = 4$). (C) Tumor growth curves and (D) body weight data of mice after NIR-II PTT operations (**$p < 0.01$, $n = 4$).**

and a significant difference ($p < 0.001$) of PA intensity could be observed between tumor and normal tissue images. Besides, *in vivo* and *ex vivo* biodistribution analysis (Figure S6) by systematic administration of fluorescent dye (Cy7) labeled SHT further validated the superior tumor accumulation efficacy of this nanotheranostics due to the effects of both the enhanced permeability and retention (EPR) and the feature of folate-mediated tumor targeting.[53,54] Although the PA intensity in the tumor decreased over time attributed to metabolism and clearance, there are still detectable PA signals after 24 h. This phenomenon was consistent with our previous results that tumorous acidity significantly enhanced the stability of CTC generated by the H_2O_2/SHT response. In contrast, the CTC would be degraded under physiological conditions (pH 7.4).[37] These data demonstratively proved that SHT could be used for NIR-II PA tumor detection based on the specific microenvironmental-H_2O_2-activated strategy.

In light of the tumor PAT results, the PTT capability and efficacy were investigated in the 4T1 xenograft tumor model. The maximum NIR-II PA signals in the tumor region could be detected at 4 h post SHT injection. PTT was conducted accordingly with a 1064 nm laser irradiation (1.0 W/cm^2) for 6 min, and the heating process was monitored every minute by an IR camera. The tumor temperature with SHT-treated mice gradually increased from the lowest at 31.2 °C to the maximum at 52.9 °C during the photoirradiation, which was significantly higher than that of saline-treated mice, with a plateau temperature of 37.4 °C (Figure 5A and B). Considering the threshold temperature (43 °C) of PTT,[55] this temperature change generated by H_2O_2-activated SHT was high enough to induce tumor ablation. To evaluate the antitumor effect for the NIR-II PTT using SHT, tumor volumes were continuously monitored for 2 weeks. As indicated in Figures 5C and S7, the growth of tumors for SHT-treated mice was significantly suppressed without reoccurrence observed after 1064 nm photoirradiation. In contrast, saline-treated mice with the same irradiation failed to show any antitumor capability. Besides, no notable therapeutic effect was found for both SHT and saline-treated mice without NIR-II laser irradiation. These results showed that SHT offers excellent activatable photothermal therapeutic ability against tumors. Moreover, there was no obvious body weight loss observed for all the mice throughout the experimental period (Figure 5D). Additionally, the histological studies by using TUNEL and H&E staining methods were carried out to further evaluate the PTT outcomes and potential side effects.[56,57] As expected, no appreciable histopathological damage or inflammation could be observed in hearts, livers, spleens, and kidneys of both SHT- and saline-treated mice with or without NIR-II laser irradiation (Figure S8). In contrast, compared to saline-treated tumor tissues or free NIR-II laser irradiated groups, tumor tissues in the SHT-treated group after PTT indicated obvious damage (Figure S9). Most importantly, the TUNEL staining of tumor tissues also indicated apoptotic tumor cells for SHT-treated mice after PTT, while no noticeable apoptosis could be observed for saline-treated mice after laser irradiation. Further serum biochemical tests of SHT-administrated mice indicated that the pathological indicators of both liver (*e.g.*, ALT, AST, ALP) and kidney (*e.g.*, CREA, BUN, LDH) were all in the normal range in comparison to the control (Figure S10). These data validated that the SHT-mediated microenvironmental activatable NIR-II PTT exhibited a highly specific and effective tumor therapeutic action along with good biosafety.

CONCLUSION

In conclusion, we have successfully developed a microenvironmental stimuli-activatable nanotheranostics (SHT) for PA tumor detection and combined PTT both in the NIR-II optical window. Such a smart phototheranostics showed highly sensitive H_2O_2-activated/acid-enhanced PA signal changes as

DOI: 10.1021/acsnano.9b01411
ACS Nano 2019, 13, 5816−5825

well as precision PTT *in vitro* and *in vivo*, which significantly minimized the nonspecific signal readout and therapeutic side effects encountered in the conventional "always-on" theranostic agents. Most importantly, the NIR-II light-mediated tumor PAT and PTT eventually led to superior deep-tissue photoacoustic contrast and photothermal heating capabilities in living mice. In view of the numerous merits of stimuli-activatable NIR-II photo-nanotheranostics, this study provides great opportunities for the investigation and management of redox/acid-associated (patho)physiological alterations, as well as contributing to the development of future nanomedicine.[58]

METHODS

Preparation of Mesoporous Silica Nanoparticles (MSNs). The dendritic MSNs were prepared following the previous reported one-pot biphase stratification approach.[42] Typically, 12 mL of (25 wt %) cetyltrimethylammonium chloride (CTAC) solution and 45 μL of triethylamine (TEA) were added to 18 mL of DI water and stirred gently at 60 °C for 1 h in a 100 mL round-bottom flask. Then 5 mL of (5 v/v %) tetraethoxysilane in cyclohexane was carefully added to the water−CTAC−TEA solution and kept at 60 °C in an oil bath under slow stirring (~100 rpm) for 30 min. Then 1 mL of (10 v/v %) (3-aminopropyl)triethoxysilane in cyclohexane was drop-wisely added and kept at a constant temperature with continuous stirring for another 6 h. The products were collected by centrifugation (5000 rpm, 5 min) and washed three times with ethanol to remove the residual reactants. Finally, the collected products were extracted with a 3 mg/mL ammonium nitrate (NH_4NO_3) ethanol solution at 60 °C for 6 h twice to remove the template. The obtained dendritic MSNs can be stored in ethanol solution in 4 °C for the subsequent experiments.

Modification and TMB/HRP Loading of MSNs. The folic-acid-functionalized MSNs were prepared following a reported method.[43] Briefly, the folic acid (10 mg) was first activated by N-hydroxysuccinimide esterification of FA (22 mg, 0.05 mmol) with *N*-hydroxysuccinimide (NHS) (5.8 mg, 0.05 mmol) in 2 mL of dry DMSO solution of 1-ethyl-3-(3-dimethylaminopropyl)carbodiimide (19 mg, 0.1 mmol), hydroxybenzotriazole (9 mg, 0.07 mmol), and 20 μL of *N*,*N*-diisopropylethylamine. The mixture was stirred for 30 min at room temperature. Then, the MSN−NH_2 suspension (20 mg in 3 mL of DMSO) was dropped into the NHS−FA solution and stirred for 24 h. Finally, the reaction mixture was collected by centrifugation (5000 rpm, 5 min) and washed with DMSO and DI water several times, respectively, to afford FA-MSNs. For the TMB loading, 1 mL of FA-MSNs suspension (10 mg/mL) was added in 1 mL of 0.1 M TMB water solution, which was sonicated for 10 min and then stirred for 12 h under a N_2 gas atmosphere. The mixture was washed with DI water two times to produce TMB-loaded MSNs. For the HRP (Sigma-Aldrich) loading, 10 mg of as-prepared TMB-MSNs was redispersed in 2 mL of acetic acid−sodium acetate buffer (pH = 5.0) containing 1 mg of HRP. The mixed solution was then kept at 4 °C with gentle stirring for 12 h. The TMB/HRP-loaded MSNs (SHT) were obtained by centrifugation (5000 rpm, 5 min) after washing with DI water. The products were stored at 4 °C for further use. In all modification and loading processes, the loading efficacy was quantified by the TMB/HRP/H_2O_2 absorbance response with UV−vis spectroscopy measurements.

Characterization and Measurements. TEM images were recorded using a FEI EM208S TEM (Philips) operated at 100 kV. DLS measurement was performed by a Brookhaven 90 Plus nanoparticle size analyzer. UV−vis−NIR absorption spectra were measured using a Perkim Elmer Lambda 950 spectrometer, and a Bruker Vertex 80v vacuum FTIR spectrometer was used to study the material modifications.

Specific and Quantitative Detection of H_2O_2. To study the specificity of H_2O_2 detection, 0.1 mg/mL SHT was incubated with various reactive oxygen species (25 μM) for 10 min with gentle shaking. Then, the UV−vis−NIR absorption spectra of the mixtures after incubation were measured. To study the pH-sensitivity, SHT and H_2O_2 were added in phosphate-buffered saline (PBS) buffers with different pH values, and the colorimetric test was subsequently performed following the same procedure. For the quantitative analysis, different concentrations of H_2O_2 were incubated with SHT for 10 min, and then the absorbance and photoacoustic signals were measured at 1064 nm.

In Vitro NIR-II PAT and PT Studies. NIR-II PA signals of SHT with different concentrations of H_2O_2 were measured and plotted by the homemade PAT instrumentation (Figure 4B) with a Q-switched Nd:YAG pump laser at 1064 nm, 5 ns, 10 Hz as the light source. Samples were placed inside low-density polyethylene (LDPE) tubes with an inner diameter (i.d.) of 0.59 mm and outer diameter (o.d.) of 0.78 mm. A single-element ultrasound transducer (UST, V323-SU/2.25 MHz, 13 mm active area, and 70% nominal bandwidth, Panametrics) was immersed in water for coupling of PA signals to the UST. The sample was irradiated with 1064 nm laser pulses, and PA signals were detected by UST, amplified with a gain of 50 dB, and subsequently band-pass filtered (1−10 MHz) by a receiver/filter/amplifier (RFA) unit. Finally, the output signals from the RFA unit were digitized with a data acquisition card (GaGe, Compuscope 4227) operated at 25 MHz, and the acquired signals were stored in the computer. For the NIR-II photothermal test, SHT solutions (200 μL, 0.1 mg/mL) with H_2O_2 in different pH PBS buffers were irradiated by a 1064 nm laser with a power density of 1 W/cm^2. The temperature changes were monitored every 20 s by an IR thermal camera (FLIR) during both the photothermal heating (0−3 min) and the cooling period (3−8 min). The photostability study of SHT with 50 μM H_2O_2 was also evaluated by 1064 nm laser irradiation (1 W/cm^2) for five repetitions.

Deep-Tissue NIR-II PAT and PT Studies. For the deep-tissue PAT study, 100 μL of SHT (1 mg/mL) after 50 μM H_2O_2 activation was first embedded in a sample phantom. Then chicken breast tissues were stacked layer by layer above the phantom to obtain various imaging depths (0−4 cm). The homemade PAT setup was used for deep-tissue imaging with both typical NIR-I (800 nm) and NIR-II (1064 nm) laser sources. Finally, the acquired PA signals were used to reconstruct the image using a delay-and-sum back projection algorithm. The deep-tissue photothermal studies with both 808 and 1064 nm laser irradiations were performed following a previously reported method.[16] Typically, a 200 μL SHT solution with 50 μM H_2O_2 was filled in a 96-well plate and covered by chicken breast tissue of various thicknesses (0, 2.5, 5, and 10 mm) and then exposed to an 808 or 1064 nm laser (1 W/cm^2) for 10 min. The temperature changes of the sample under the chicken breast tissue were monitored by an IR thermal camera.

Cell Culture and Viability Test. The 4T1 cancer cell line was purchased from American Type Culture Collection (ATCC, Manassas, VA, USA), and it was cultured in Dulbecco's modified Eagle's medium (DMEM) with 10% fetal bovine serum (FBS) containing penicillin (100 IU/mL) and streptomycin (100 μg/mL) and maintained in an atmosphere containing 5% CO_2 and 95% humidified air at 37 °C. For the cytotoxicity assay, cells were seeded in 96-well plates (8000 cells/well in 100 μL) and incubated overnight. Then different concentrations of SHT were added to the cell culture medium, respectively, and the cells were incubated for 24 h. The medium was then removed and washed with PBS. Fresh cell culture medium containing TOX8 was added to the wells, and the plate was incubated for another 3 h. The fluorescence at 590 nm was measured by a Tecan's Infinite M200 microplate reader with 560 nm excitation. Cell viability was expressed by the ratio of the fluorescence of cells incubated with SHT to that of control cells.

Live/Dead Cell Staining and Hsp70-Expression Study. For live/dead cell staining, 4T1 cells were seeded in an eight-well dish (Ibidi) at a concentration of 2 × 10^4 cells/mL (0.3 mL) and incubated for 24 h. Then 0.1 mg/mL of SHT was added in the wells and incubated for another 4 h, then washed and treated with 50 μM H_2O_2 or H_2O_2-free medium. After 1 h of incubation, the cells were irradiated with a 1064 nm laser (1.0 W/cm^2) for 6 min. The control groups without NIR-II irradiation were performed. The cells were

DOI: 10.1021/acsnano.9b01411
ACS Nano 2019, 13, 5816−5825

incubated overnight and then stained with calcein AM and propidium iodide (PI) for 30 min, washed with PBS, and then imaged by a Carl Zeiss LSM 800 confocal laser microscope (Germany). Additionally, the cell viability was also measured by using a TOX-8 assay kit. For Hsp70-expression study, the 4T1 cells irradiated by a 1064 nm laser (1.0 W/cm^2, 6 min) were incubated for another 3 h; then the medium was removed and washed with PBS. Subsequently, 4T1 cells were fixed with 4% paraformaldehyde solution for 20 min. After washing three times with PBS, the cells were stained with anti-Hsp70 antibody conjugated with Alexa Fluor 488 (Biolegend Alexa Fluor 488 anti-Hsp70) and Hoechst 33258 at room temperature for 30 min. Finally, stained cells were washed with PBS again and imaged with the confocal laser microscope.

Animal Model. All animal experiments were performed in compliance with the Guidelines established by the Institutional Animal Care and Use Committee (IACUC), Sing Health. To establish the tumor model in female NCr nude mice, two million 4T1 cells suspended in 0.2 mL of DMEM (10% FBS, 1% antibiotics) were subcutaneously injected into one side of the back of mice. *In vivo* NIR-II PTT was performed when the subcutaneous tumor volume reached approximately 100 mm^3, while tumor-bearing mice with an average tumor size around 1000 mm^3 were used for NIR-II PAI.

In Vivo Tumor NIR-II PAT. *In vivo* tumor PAT was acquired by the homemade 1064 nm PAT system mentioned above. A layer of ultrasonic coupling gel was applied on the mouse's skin at the tumor area. The mouse was subsequently anesthetized and placed into the PA setup with the tumor protruding above the water tank through a hole that was sealed by transparent polyethylene film. The tumor-bearing mice were monitored and imaged before and after tail vein injection of SHT (2 mg/mL, 200 μL per mouse, n = 3) using the 1064 nm laser with a power intensity of 5.5 mJ/cm^2. At different times postinjection, PA images were acquired and reconstructed for the tumor and the normal tissue.

In Vivo Tumor NIR-II PTT. The mice bearing 4T1 xenograft tumors were administered with SHT (2 mg/mL, 200 μL) or saline (200 μL) *via* tail vein injection (n = 4). According to the PAT results, at 4 h postinjection, tumor regions of living mice were irradiated with the 1064 nm laser at 1 W/cm^2 for 6 min. An IR thermal camera was used to monitor the temperature changes of the tumor region every 1 min during laser irradiation. After the photothermal treatment, the sizes of tumors and mice body weights were measured by a caliper every other day for 2 weeks.

Histological Analysis. After NIR-II PTT and observations, mice were sacrificed (n = 4) and organs (livers, spleens, kidneys, lungs, and tumors) were fixed in 4% paraformaldehyde solution. Then paraffin-embedded sectioning was performed, and hematoxylin and eosin (H&E) staining was carried out according to standard protocols.[57] As for the terminal deoxyribonucleotide transferase-mediated nick-end labeling (TUNEL) assay,[56] the ApopTag plus peroxidase *in situ* apoptosis detection kit (Merck) was used according to the manufacturer's instructions. Images of slices were captured by a Nikon ECLIPSE 80i microscope.

Statistical Analysis. Mean PA signals of *in vitro* sample test and *in vivo* tumor detection were measured by region of interest (ROI) analysis using Matlab. Results are expressed as the mean ± SD deviation unless otherwise stated. The results were plotted by OringinPro 8.5 software, and statistical analyses were performed using the t test.

ASSOCIATED CONTENT

Supporting Information

The Supporting Information is available free of charge on the ACS Publications website at DOI: 10.1021/acsnano.9b01411.

Supplemental experimental methods, figures, and spectrum (PDF)

AUTHOR INFORMATION

Corresponding Authors

*E-mail: kypu@ntu.edu.sg.
*E-mail: bengang@ntu.edu.sg.

ORCID

Kanyi Pu: 0000-0002-8064-6009
Bengang Xing: 0000-0002-8391-1234

Notes

The authors declare no competing financial interest.

ACKNOWLEDGMENTS

B.X. acknowledges the financial support from NTU-AIT-MUV NAM/16001, Tier 1 RG5/18 (S), RG110/16 (S), SSIJRI (203-A018003), MOE 2017-T2-2-110, NTU-JSPS JRP grant (M4082175.110), and Merlion 2017 program (M408110000) awarded in Nanyang Technological University (NTU). K.P. thanks Nanyang Technological University (Start-Up grant: NTU-SUG: M4081627.120) and Singapore Ministry of Education Academic Research Fund Tier 1 (RG133/15 M4011559, 2017-T1-002-134-RG147/17) and Tier 2 (MOE 2016-T2-1-098 and MOE 2018-T2-2-042). M.P. thanks the Singapore Ministry of Health's National Medical Research Council (NMRC/OFIRG/0005/2016: M4062012) for financial support.

REFERENCES

(1) Shanmugam, V.; Selvakumar, S.; Yeh, C.-S. Near-Infrared Light-Responsive Nanomaterials in Cancer Therapeutics. *Chem. Soc. Rev.* **2014**, *43*, 6254−6287.

(2) Kim, H.; Chung, K.; Lee, S.; Kim, D. H.; Lee, H. Near-Infrared Light-Responsive Nanomaterials for Cancer Theranostics. *Wiley Interdiscip Rev. Nanomed Nanobiotechnol* **2016**, *8*, 23−45.

(3) Wang, C.; Cheng, L.; Liu, Z. Upconversion Nanoparticles for Photodynamic Therapy and Other Cancer Therapeutics. *Theranostics* **2013**, *3*, 317.

(4) Yang, G.; Liu, J.; Wu, Y.; Feng, L.; Liu, Z. Near-Infrared Light-Responsive Nanoscale Drug Delivery Systems for Cancer Treatment. *Coord. Chem. Rev.* **2016**, *320*, 100−117.

(5) Ai, X.; Mu, J.; Xing, B. Recent Advances of Light-Mediated Theranostics. *Theranostics* **2016**, *6*, 2439.

(6) Ai, X.; Ho, C. J. H.; Aw, J.; Attia, A. B. E.; Mu, J.; Wang, Y.; Wang, X.; Wang, Y.; Liu, X.; Chen, H.; et al. *In Vivo* Covalent Cross-Linking of Photon-Converted Rare-Earth Nanostructures for Tumour Localization and Theranostics. *Nat. Commun.* **2016**, *7*, 10432.

(7) Yang, Y.; Shao, Q.; Deng, R.; Wang, C.; Teng, X.; Cheng, K.; Cheng, Z.; Huang, L.; Liu, Z.; Liu, X.; et al. *In Vitro* and *In Vivo* Uncaging and Bioluminescence Imaging by Using Photocaged Upconversion Nanoparticles. *Angew. Chem., Int. Ed.* **2012**, *51*, 3125−3129.

(8) Huang, P.; Lin, J.; Li, W.; Rong, P.; Wang, Z.; Wang, S.; Wang, X.; Sun, X.; Aronova, M.; Niu, G. Biodegradable Gold Nanovesicles with an Ultrastrong Plasmonic Coupling Effect for Photoacoustic Imaging and Photothermal Therapy. *Angew. Chem., Int. Ed.* **2013**, *52*, 13958−13964.

(9) Cheng, L.; Liu, J.; Gu, X.; Gong, H.; Shi, X.; Liu, T.; Wang, C.; Wang, X.; Liu, G.; Xing, H. PEGylated WS_2 Nanosheets as a Multifunctional Theranostic Agent for *In Vivo* Dual-Modal CT/Photoacoustic Imaging Guided Photothermal Therapy. *Adv. Mater.* **2014**, *26*, 1886−1893.

(10) Lyu, Y.; Fang, Y.; Miao, Q.; Zhen, X.; Ding, D.; Pu, K. Intraparticle Molecular Orbital Engineering of Semiconducting Polymer Nanoparticles as Amplified Theranostics for *In Vivo* Photoacoustic Imaging and Photothermal Therapy. *ACS Nano* **2016**, *10*, 4472−4481.

DOI: 10.1021/acsnano.9b01411
ACS Nano 2019, 13, 5816−5825

(11) Zou, L.; Wang, H.; He, B.; Zeng, L.; Tan, T.; Cao, H.; He, X.; Zhang, Z.; Guo, S.; Li, Y. Current Approaches of Photothermal Therapy in Treating Cancer Metastasis with Nanotherapeutics. *Theranostics* **2016**, *6*, 762.
(12) Upputuri, P. K.; Pramanik, M. Recent Advances toward Preclinical and Clinical Translation of Photoacoustic Tomography: A Review. *J. Biomed. Opt.* **2017**, *22*, 041006.
(13) Guo, B.; Sheng, Z.; Hu, D.; Liu, C.; Zheng, H.; Liu, B. Through Scalp and Skull NIR-II Photothermal Therapy of Deep Orthotopic Brain Tumors with Precise Photoacoustic Imaging Guidance. *Adv. Mater.* **2018**, *30*, 1802591.
(14) Zhou, J.; Jiang, Y.; Hou, S.; Upputuri, P. K.; Wu, D.; Li, J.; Wang, P.; Zhen, X.; Pramanik, M.; Pu, K. Compact Plasmonic Blackbody for Cancer Theranosis in the Near-Infrared II Window. *ACS Nano* **2018**, *12*, 2643−2651.
(15) Ding, X.; Liow, C. H.; Zhang, M.; Huang, R.; Li, C.; Shen, H.; Liu, M.; Zou, Y.; Gao, N.; Zhang, Z. Surface Plasmon Resonance Enhanced Light Absorption and Photothermal Therapy in the Second Near-Infrared Window. *J. Am. Chem. Soc.* **2014**, *136*, 15684−15693.
(16) Jiang, Y.; Li, J.; Zhen, X.; Xie, C.; Pu, K. Dual-Peak Absorbing Semiconducting Copolymer Nanoparticles for First and Second Near-Infrared Window Photothermal Therapy: A Comparative Study. *Adv. Mater.* **2018**, *30*, 1705980.
(17) Huang, K.; Zhang, Y.; Lin, J.; Huang, P. Nanomaterials for Photoacoustic Imaging in Second Near-Infrared Window. *Biomater. Sci.* **2019**, *7*, 472−479.
(18) Wang, X.; Ma, Y.; Sheng, X.; Wang, Y.; Xu, H. Ultrathin Polypyrrole Nanosheets *via* Space-Confined Synthesis for Efficient Photothermal Therapy in the Second Near-Infrared Window. *Nano Lett.* **2018**, *18*, 2217−2225.
(19) Vijayaraghavan, P.; Liu, C. H.; Vankayala, R.; Chiang, C. S.; Hwang, K. C. Designing Multi-Branched Gold Nanoechinus for NIR Light Activated Dual Modal Photodynamic and Photothermal Therapy in the Second Biological Window. *Adv. Mater.* **2014**, *26*, 6689−6695.
(20) Zhang, D.; Xu, H.; Zhang, X.; Liu, Y.; Wu, M.; Li, J.; Yang, H.; Liu, G.; Liu, X.; Liu, J. Self-Quenched Metal−Organic Particles as Dual-Mode Therapeutic Agents for Photoacoustic Imaging-Guided Second Near-Infrared Window Photochemotherapy. *ACS Appl. Mater. Interfaces* **2018**, *10*, 25203−25212.
(21) Zhao, D.-H.; Yang, J.; Xia, R.-X.; Yao, M.-H.; Jin, R.-M.; Zhao, Y.-D.; Liu, B. High Quantum Yield Ag_2S Quantum Dot @ Polypeptide-Engineered Hybrid Nanogels for Targeted Second Near-Infrared Fluorescence/Photoacoustic Imaging and Photothermal Therapy. *Chem. Commun.* **2018**, *54*, 527−530.
(22) Cao, Z.; Feng, L.; Zhang, G.; Wang, J.; Shen, S.; Li, D.; Yang, X. Semiconducting Polymer-Based Nanoparticles with Strong Absorbance in NIR-II Window for *In Vivo* Photothermal Therapy And Photoacoustic Imaging. *Biomaterials* **2018**, *155*, 103−111.
(23) Yu, X.; Yang, K.; Chen, X.; Li, W. Black Hollow Silicon Oxide Nanoparticles as Highly Efficient Photothermal Agents in the Second Near-Infrared Window for *In Vivo* Cancer Therapy. *Biomaterials* **2017**, *143*, 120−129.
(24) Jiang, Y.; Upputuri, P. K.; Xie, C.; Zeng, Z.; Sharma, A.; Zhen, X.; Li, J.; Huang, J.; Pramanik, M.; Pu, K. Metabolizable Semiconducting Polymer Nanoparticles for Second Near-Infrared Photoacoustic Imaging. *Adv. Mater.* **2019**, *31*, 1808166.
(25) Upputuri, P. K.; Pramanik, M. Photoacoustic Imaging in the Second Near-Infrared Window: A Review. *J. Biomed. Opt.* **2019**, *24*, 040901.
(26) Melancon, M. P.; Zhou, M.; Li, C. Cancer Theranostics with Near-Infrared Light-Activatable Multimodal Nanoparticles. *Acc. Chem. Res.* **2011**, *44*, 947−956.
(27) Lim, E.-K.; Kim, T.; Paik, S.; Haam, S.; Huh, Y.-M.; Lee, K. Nanomaterials for Theranostics: Recent Advances and Future Challenges. *Chem. Rev.* **2015**, *115*, 327−394.
(28) Yue, X.; Zhang, Q.; Dai, Z. Near-Infrared Light-Activatable Polymeric Nanoformulations for Combined Therapy and Imaging of Cancer. *Adv. Drug Delivery Rev.* **2017**, *115*, 155−170.
(29) Joyce, J. A. Therapeutic Targeting of the Tumor Microenvironment. *Cancer Cell* **2005**, *7*, 513−520.
(30) Mbeunkui, F.; Johann, D. J. Cancer and the Tumor Microenvironment: A Review of an Essential Relationship. *Cancer Chemother. Pharmacol.* **2009**, *63*, 571−582.
(31) Sounni, N. E.; Noel, A. Targeting the Tumor Microenvironment for Cancer Therapy. *Clin. Chem.* **2013**, *59*, 85−93.
(32) Khawar, I. A.; Kim, J. H.; Kuh, H.-J. Improving Drug Delivery to Solid Tumors: Priming the Tumor Microenvironment. *J. Controlled Release* **2015**, *201*, 78−89.
(33) Khramtsov, V. V.; Gillies, R. J. Janus-Faced Tumor Microenvironment and Redox. *Antioxid. Redox Signaling* **2014**, *21*, 723−729.
(34) Shi, B.; Yan, Q.; Tang, J.; Xin, K.; Zhang, J.; Zhu, Y.; Xu, G.; Wang, R.; Chen, J.; Gao, W. Hydrogen Sulfide-Activatable Second Near-Infrared Fluorescent Nanoassemblies for Targeted Photothermal Cancer Therapy. *Nano Lett.* **2018**, *18*, 6411−6416.
(35) Jeong, S.; Song, J.; Lee, W.; Ryu, Y. M.; Jung, Y.; Kim, S.-Y.; Kim, K.; Hong, S. C.; Myung, S. J.; Kim, S. Cancer-Microenvironment-Sensitive Activatable Quantum Dot Probe in the Second Near-Infrared Window. *Nano Lett.* **2017**, *17*, 1378−1386.
(36) Meng, X.; Zhang, J.; Sun, Z.; Zhou, L.; Deng, G.; Li, S.; Li, W.; Gong, P.; Cai, L. Hypoxia-Triggered Single Molecule Probe for High-Contrast NIR-II/PA Tumor Imaging and Robust Photothermal Therapy. *Theranostics* **2018**, *8*, 6025.
(37) Wang, Z.; Upputuri, P. K.; Zhen, X.; Zhang, R.; Jiang, Y.; Ai, X.; Zhang, Z.; Hu, M.; Meng, Z.; Lu, Y.; Zheng, Y.; Pu, K.; Pramanik, M.; Xing, B. pH-Sensitive and Biodegradable Charge-Transfer Nanocomplex for Second Near-Infrared Photoacoustic Tumor Imaging. *Nano Res.* **2019**, *12*, 49−55.
(38) Lennicke, C.; Rahn, J.; Lichtenfels, R.; Wessjohann, L. A.; Seliger, B. Hydrogen Peroxide−Production, Fate and Role in Redox Signaling of Tumor Cells. *Cell Commun. Signaling* **2015**, *13*, 39.
(39) López-Lázaro, M. Dual Role of Hydrogen Peroxide in Cancer: Possible Relevance to Cancer Chemoprevention and Therapy. *Cancer Lett.* **2007**, *252*, 1−8.
(40) Kato, Y.; Ozawa, S.; Miyamoto, C.; Maehata, Y.; Suzuki, A.; Maeda, T.; Baba, Y. Acidic Extracellular Microenvironment and Cancer. *Cancer Cell Int.* **2013**, *13*, 89.
(41) Josephy, P. D.; Eling, T.; Mason, R. P. The Horseradish Peroxidase-Catalyzed Oxidation of 3, 5, 3′, 5′-Tetramethylbenzidine. Free Radical and Charge-Transfer Complex Intermediates. *J. Biol. Chem.* **1982**, *257*, 3669−3675.
(42) Shen, D.; Yang, J.; Li, X.; Zhou, L.; Zhang, R.; Li, W.; Chen, L.; Wang, R.; Zhang, F.; Zhao, D. Biphase Stratification Approach to Three-Dimensional Dendritic Biodegradable Mesoporous Silica Nanospheres. *Nano Lett.* **2014**, *14*, 923−932.
(43) Lu, J.; Li, Z.; Zink, J. I.; Tamanoi, F. *In Vivo* Tumor Suppression Efficacy of Mesoporous Silica Nanoparticles-Based Drug-Delivery System: Enhanced Efficacy by Folate Modification. *Nanomedicine* **2012**, *8*, 212−220.
(44) Vallet-Regí, M.; Balas, F.; Arcos, D. Mesoporous Materials for Drug Delivery. *Angew. Chem., Int. Ed.* **2007**, *46*, 7548−7558.
(45) Popat, A.; Hartono, S. B.; Stahr, F.; Liu, J.; Qiao, S. Z.; Lu, G. Q. M. Mesoporous Silica Nanoparticles for Bioadsorption, Enzyme Immobilisation, and Delivery Carriers. *Nanoscale* **2011**, *3*, 2801−2818.
(46) John Goka, A.; Farthing, M. J. The Use of 3, 3′, 5, 5′-Tetramethylbenzidine as a Peroxidase Substrate in Microplate Enzyme-Linked Immunosorbent Assay. *J. Immunoassay* **1987**, *8*, 29−41.
(47) Vaupel, P.; Kallinowski, F.; Okunieff, P. Blood Flow, Oxygen and Nutrient Supply, and Metabolic Microenvironment of Human Tumors: A Review. *Cancer Res.* **1989**, *49*, 6449−6465.
(48) Corbet, C.; Feron, O. Tumour Acidosis: From the Passenger to the Driver's Seat. *Nat. Rev. Cancer* **2017**, *17*, 577−593.
(49) Fu, G.; Sanjay, S. T.; Zhou, W.; Brekken, R. A.; Kirken, R. A.; Li, X. Exploration of Nanoparticle-Mediated Photothermal Effect of TMB-H_2O_2 Colorimetric System and Its Application in a Visual

DOI: 10.1021/acsnano.9b01411
ACS Nano 2019, 13, 5816−5825

Quantitative Photothermal Immunoassay. *Anal. Chem.* **2018**, *90*, 5930−5937.
(50) Hildebrandt, B.; Wust, P.; Ahlers, O.; Dieing, A.; Sreenivasa, G.; Kerner, T.; Felix, R.; Riess, H. The Cellular and Molecular Basis of Hyperthermia. *Crit. Rev. Oncol./Hematol.* **2002**, *43*, 33−56.
(51) Ariyasu, S.; Mu, J.; Zhang, X.; Huang, Y.; Yeow, E. K. L.; Zhang, H.; Xing, B. Investigation of Thermally Induced Cellular Ablation and Heat Response Triggered by Planar MoS_2-Based Nanocomposite. *Bioconjugate Chem.* **2017**, *28*, 1059−1067.
(52) Pulaski, B. A.; Ostrand-Rosenberg, S.Mouse 4T1 Breast Tumor Model*Curr. Protoc. Immunol.***2001***39* DOI: 10.1002/0471142735.im2002s39
(53) Iyer, A. K.; Khaled, G.; Fang, J.; Maeda, H. Exploiting the Enhanced Permeability and Retention Effect for Tumor Targeting. *Drug Discovery Today* **2006**, *11*, 812−818.
(54) Lu, Y.; Low, P. S. Folate-Mediated Delivery of Macromolecular Anticancer Therapeutic Agents. *Adv. Drug Delivery Rev.* **2012**, *64*, 342−352.
(55) Melamed, J. R.; Edelstein, R. S.; Day, E. S. Elucidating the Fundamental Mechanisms of Cell Death Triggered by Photothermal Therapy. *ACS Nano* **2015**, *9*, 6−11.
(56) Kraupp, B. G.; Ruttkay-Nedecky, B.; Koudelka, H.; Bukowska, K.; Bursch, W.; Schulte -Hermann, R. *In Situ* Detection of Fragmented DNA (Tunel Assay) Fails to Discriminate among Apoptosis, Necrosis, and Autolytic Cell Death: A Cautionary Note. *Hepatology* **1995**, *21*, 1465−1468.
(57) Fischer, A. H.; Jacobson, K. A.; Rose, J.; Zeller, R. Hematoxylin and Eosin Staining of Tissue and Cell Sections. *Cold Spring Harb. Protoc.* **2008**, *5*, prot4986.
(58) Youn, Y. S.; Bae, Y. H. Perspectives on the Past, Present, and Future of Cancer Nanomedicine. *Adv. Drug Delivery Rev.* **2018**, *130*, 3−11.

DOI: 10.1021/acsnano.9b01411
ACS Nano 2019, 13, 5816−5825